Physica Scripta

INCLUSIVE PUBLISHING TRUSTED SCIENCE

PURPOSE-LED PUBLISHING™

PAPER • **OPEN ACCESS**

Ultra-compact broadband graphene-based terahertz metamaterial absorber with refractive index sensing capability

To cite this article: Kayhan Çelik 2026 *Phys. Scr.* **101** 325908

View the article online for updates and enhancements.

You may also like

- Design of a tunable terahertz metamaterial absorber for compact multifunctional communication and biosensing platforms
Manish Rai, Anup Kumar, Manoranjan Kumar et al.
- Design of metasurface absorber with four unequal rectangular rings for ultrawide THz bandwidth
Farzana Yeasmin, Md Aslam Mollah and Sk Md Abdul Kaium
- Inverse design of high-performance coding met-amaterial absorbers driven by NSGA-II
Senfeng Lai, Bingye Zhou, Huiyuan Fu et al.

This content was downloaded from IP address 194.27.6.19 on 24/08/2026 at 23:11

Physica Scripta

Check for updates

OPEN ACCESS

RECEIVED
20 April 2026

REVISED
22 June 2026

ACCEPTED FOR PUBLICATION
30 July 2026

PUBLISHED
10 August 2026

Original content from this work may be used under the terms of the Creative Commons Attribution 4.0 licence.

Any further distribution of this work must maintain attribution to the author(s) and the title of the work, journal citation and DOI.

PAPER

Ultra-compact broadband graphene-based terahertz metamaterial absorber with refractive index sensing capability

Kayhan Çelik*

Department of Electrical and Electronics Engineering, Technology Faculty, Gazi University, Ankara 06560, Türkiye
* Author to whom any correspondence should be addressed.

E-mail: kayhancelik1923@gmail.com and kayhancelik@gazi.edu.tr

Keywords: metamaterial absorber, terahertz, broadband absorption, graphene, ultra-compact structure

Abstract

This paper presents an ultra-compact broadband terahertz metamaterial absorber based on graphene. The proposed structure exhibits an exceptionally small normalized size of approximately $0.067\lambda_0 \times 0.067\lambda_0 \times 0.066\lambda_0$, making it one of the most compact designs reported in the literature. Unlike many previously reported broadband absorbers that rely on complex multilayer architectures or hybrid active materials, the proposed design employs only two geometrically simple graphene resonators integrated within a three-layer configuration. Arlon 1000D dielectric layer is used to provide appropriate spacing between the resonators and the metallic ground plane, ensuring effective impedance matching, while the copper ground layer completely suppresses transmission. Broadband absorption is achieved through the coupling of multiple resonance modes generated by the resonators of different sizes. As a result, the absorber maintains an absorption level exceeding 90% over the frequency range of 2–2.93 THz. The proposed design offers a unique combination of ultra-compact size, structural simplicity, and broadband absorption performance. The absorber exhibits near polarization-insensitive performance for incident angles up to 30° and maintains stable absorption characteristics under different azimuth angles. Fabrication tolerance analyses demonstrate that the proposed design is robust against dimensional variations, confirming its suitability for practical implementation. Furthermore, the structure is investigated as a refractive-index sensor, exhibiting an average sensitivity of 143 GHz RIU^{-1} and demonstrating its multifunctional capability. Owing to its unique combination of ultra-compact size, structural simplicity, broadband absorption performance, and sensing potential, the proposed design represents a promising platform for future terahertz devices and integrated THz systems.

1. Introduction

The terahertz (THz) frequency range (0.1–10 THz) has become a research area of intense interest in recent years in many fields such as communication systems, high-resolution imaging, security scanning systems, biomedical diagnostics, and sensor applications [1, 2]. THz waves are located between the microwave and infrared regions, and play a significant role in future technologies due to both their high data carrying capacity and unique properties in material interactions [3–8]. However, one of the most important challenges encountered in systems operating in this frequency band is the effective control and direction of electromagnetic waves, and especially the suppression of unwanted reflections. The generally poor absorption of natural materials in the THz region necessitates the design of high-performance absorber structures. At this point, metamaterials stand out due to the flexibility they offer in controlling electromagnetic waves. Metamaterials are structures created using artificial units (unit cells) designed at the sub-wavelength scale and capable of exhibiting electromagnetic properties not found in nature.

Metamaterial-based absorbers, in particular, offer significant advantages over conventional absorbers due to their thin structures, high absorption efficiencies, and broadband or multiband operation capabilities. In such structures, transmission is typically reduced to zero, and reflection is minimized by using a resonator geometry in the top layer, a dielectric layer in the middle layer, and a metal substrate in

© 2026 The Author(s). Published by IOP Publishing Ltd

the bottom layer, ensuring impedance matching. Thus, a large portion of the incoming electromagnetic energy is trapped and absorbed within the structure. In recent years, graphene, a two-dimensional material, has emerged as a significant alternative in absorber designs due to its superior electrical and optical properties in the THz frequency range. Graphene's surface conductivity is dynamically controllable via the Fermi level, making absorber structures tunable. Furthermore, graphene's high surface current carrying capacity, and lossy nature allow for efficient electromagnetic energy damping. These properties make graphene-based absorbers particularly suitable for broadband and high-efficiency THz applications. Although many metamaterial absorber designs operating in the THz region have been proposed in the literature, a significant portion of these structures operate in a narrow band or present fabrication challenges due to complex geometries. Furthermore, some designs have disadvantages such as high thickness requirements or limited frequency tunability. Therefore, there is a need for new design approaches that are both thin-structured and capable of providing high absorption in a wide band. Terahertz metamaterial absorbers integrated with graphene have become a prominent topic of scientific investigation, and numerous studies on THz metamaterial absorbers have been reported in the literature. Some representative works are summarized below. A terahertz metamaterial absorber with dynamic tunability, offering both triple narrowband and broadband absorption, was reported by Yin *et al*, with absorption levels exceeding 90% in the 6.93–10.16 THz range [9]. Etman *et al* proposed a broadband VO_2-based terahertz metamaterial absorber optimized using a quadratic model-based optimization algorithm, achieving polarization-insensitive and wide-angle absorption characteristics. Wei *et al* [10] presented a graphene-based, single-layer terahertz metamaterial absorber with tunable broadband characteristics, achieved through enhanced electric-field coupling. An absorption level exceeding 90% is sustained across the 1.75–4.85 THz range. Kumar and Rao [11] presented the design and numerical analysis of an ultra-wideband terahertz metamaterial absorber, achieving a simulated bandwidth of 4.93 THz (3.44–8.37 THz) in the conducting state of VO_2. A VO_2-resonator-based metamaterial absorber aimed at cancer sensing was presented by Mohammed *et al* [12]. The proposed configuration achieves a 1.22 THz absorption bandwidth (0.8–2.19 THz), including two distinct resonances with absorption levels above 99% at 0.97 THz and 2.1 THz. Wang *et al* [13] developed a VO_2-integrated terahertz metamaterial absorber exhibiting tunability and polarization independence, with an absorption bandwidth of 6.35 THz over the 2.82–9.17 THz range. Bhatt *et al* [14] presented a broadband VO_2-based terahertz absorber achieving 90% absorption over 2.66–6.48 THz through a compact ultrathin design optimized using deep learning techniques. In another work, Babu *et al* [15] proposed a reconfigurable VO_2-based terahertz metamaterial absorber for biomedical sensing, enabling cancer cell detection through refractive index sensing and machine learning-assisted performance optimization. Mishra *et al* [16] developed a thermally reconfigurable VO_2-based absorber capable of switching between multiple microwave frequency bands through the insulator-to-metal phase transition of VO_2. Zhang *et al* [17] introduced a polarization-insensitive terahertz absorber with ultra-wideband and wide-angle performance, achieving over 90% absorption across the 2.9–12.44 THz range. In [18], Rekha *et al* developed a terahertz metasurface absorber featuring a graphene-based tunable Minkowski fractal design, exhibiting broadband and polarization-insensitive characteristics. The structure achieves dual-band absorption with efficiencies exceeding 90% across 3.34–3.98 THz and 4.6–5.30 THz. Furthermore, Chao *et al* [19] introduced a graphene-enabled broadband and tunable terahertz absorber, delivering more than 99% absorption over 3.45–4.83 THz. Significant developments have been made in terahertz metamaterial absorbers; however, integrating ultra-compact dimensions with broadband absorption, polarization independence, and angle-insensitive behavior remains challenging. The majority of existing metamaterial absorbers employ intricate architectures, such as stacked layers and enlarged unit cells, in order to realize wideband absorption. Most recent graphene-integrated metamaterial absorbers primarily focus on tunable performance, with limited consideration of structural simplicity and miniaturization. This study presents a graphene-based metamaterial absorber design operating in the frequency range of 2–2.93 THz. The 9.7 μm thick Arlon 1000D dielectric layer in the middle layer optimizes impedance matching by providing the appropriate distance between the resonator, and the metal substrate, and contributes to the reduction of reflection. The copper substrate in the bottom layer completely blocks transmission, retaining electromagnetic energy within the structure and thus maximizing absorption. The proposed design is notable for both its geometric simplicity and high-performance characteristics. Its slim structure facilitates ease of manufacturing and integration into practical applications. Furthermore, the tunability potential provided by the use of graphene allows this structure to be used in future reconfigurable or active absorber systems. In these respects, the study aims to contribute to the design of highly efficient, wideband, and compact absorbers in the THz frequency region. The remainder of this paper is organized as follows. Section 2 presents the absorber design and performance analysis, while section 3 concludes the paper.

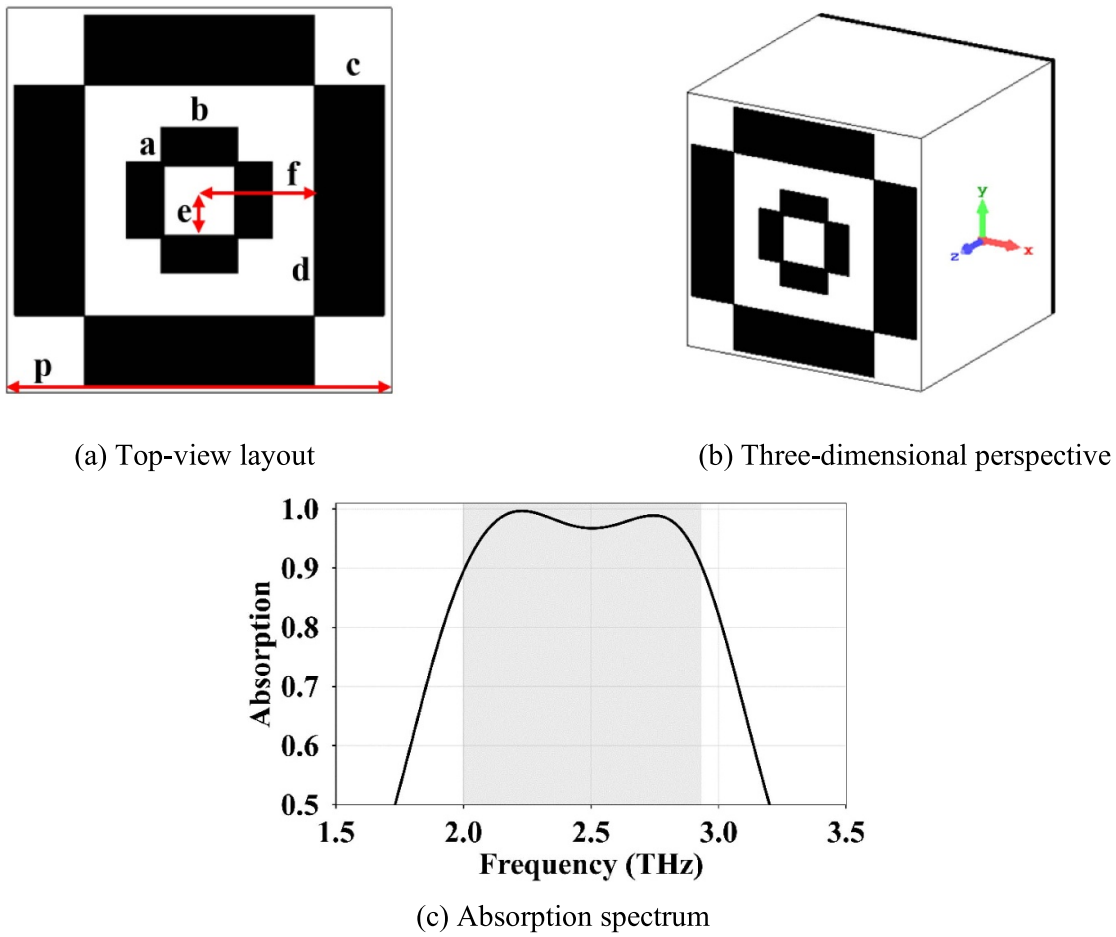


Figure 1. The proposed wideband THz absorber.

Table 1. Dimensions of the proposed absorber.

Parameter	Unit (μm)
p	10
a	1
b	2
c	1.8
d	6
e	0.9
f	3

2. Design and analysis of the graphene metamaterial absorber

2.1. Absorber configuration and operating principle

Figure 1 illustrates the overall architecture of the proposed broadband terahertz metamaterial absorber, highlighting its top-view configuration, three-dimensional representation, and absorption characteristics. The structure is relatively simple and comprises three layers, including a graphene pattern on the top, a dielectric substrate in the middle, and a metallic layer at the bottom. The parameters of the proposed absorber are given in table 1.

In the proposed design, two graphene resonators with different sizes are employed in the top layer to create different resonance modes, enabling broadband absorption. Thanks to this multi-resonance approach, the structure exhibits effective performance over a wide frequency range without being tied to a single resonance frequency. For accurate electromagnetic modeling, graphene is commonly treated as a two-dimensional sheet defined by its surface conductivity. In this study, an equivalent thin-layer approach is employed in CST Microwave Studio to model graphene. Within this method, the effective

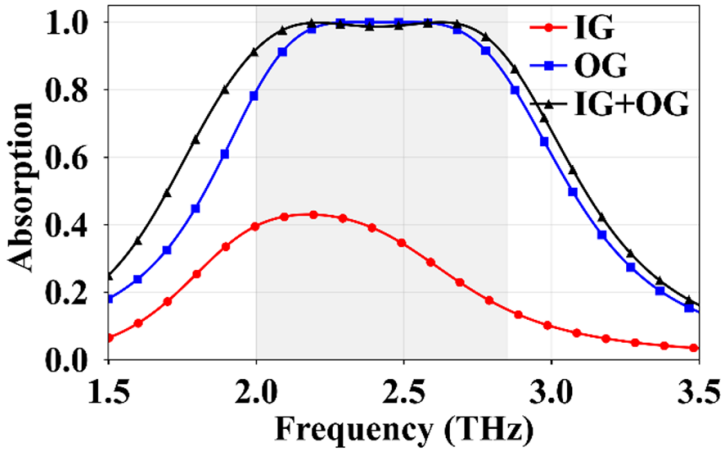


Figure 2. Absorption responses of the inner graphene resonator (IG), outer graphene resonator (OG), and their combined configuration.

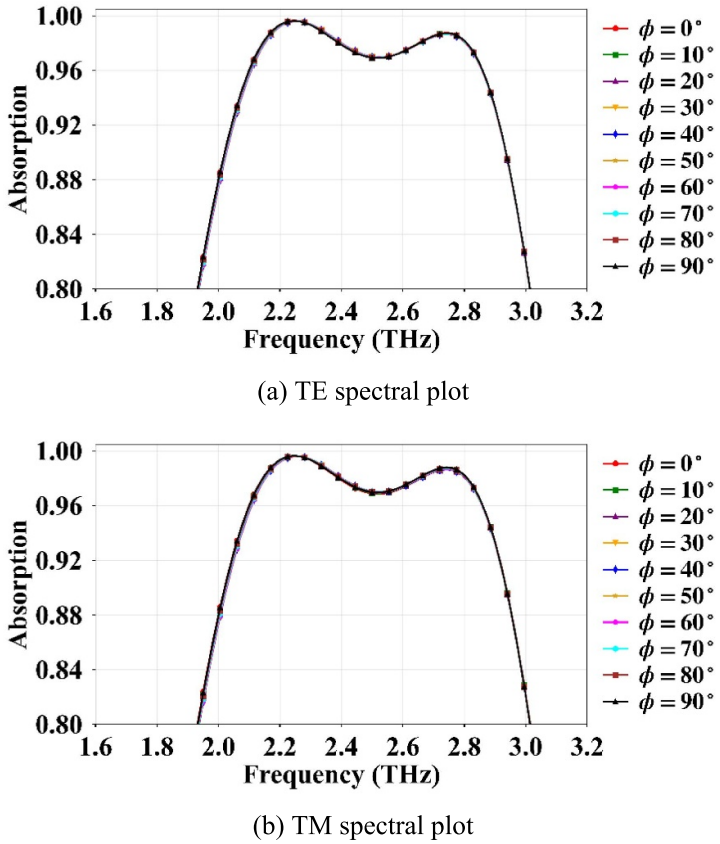
permittivity is derived from the graphene's surface conductivity using the Kubo formulation. The equivalent permittivity of graphene can be expressed as follows [20–23]:

$$\varepsilon_{\text{eff}} = 1 + \frac{j\sigma}{\omega\varepsilon_0 t}. \tag{1}$$

In this expression, σ refers to the complex surface conductivity of graphene, ω indicates the angular frequency of the incident wave, ε_0 denotes the vacuum permittivity, and t is the effective thickness assigned to the graphene layer. To emulate the surface properties of graphene, a very thin layer ($t = 0.015$ μm) is employed. This modeling approach is commonly used in CST Microwave Studio for terahertz graphene simulations. The parameters are chosen as follows: chemical potential of 0.9 eV, temperature of 300 K, and relaxation time of 0.2 ps. The 9.7 μm thick Arlon 1000D dielectric layer in the middle layer optimizes impedance matching by providing the appropriate distance between the resonator and the metal substrate, and contributes to the reduction of reflection. Arlon AD 1000 is characterized by a relative permittivity of 10.2 and a loss tangent of 0.0023. A copper ground plane with a conductivity of 5.8×10^7 S m^{-1} and a thickness of 0.2 μm is used at the bottom. Since this thickness exceeds the skin depth at the operating frequencies, electromagnetic transmission through the layer is effectively suppressed. CST Microwave Studio was utilized to design and analyze the absorber, employing its frequency-domain solver for full-wave simulations. Periodic boundaries were assigned in the x and y directions, whereas open (add space) boundaries were set along the z-axis, with excitation implemented via Floquet ports. The absorption coefficient is expressed as $A(\omega) = 1 - R(\omega) - T(\omega)$, with $R(\omega) = |S_{11}(\omega)|^2$ and $T(\omega) = |S_{21}(\omega)|^2$, representing reflection and transmission, respectively. As the thickness of the metallic layer is higher than the skin depth, the electromagnetic wave does not penetrate into that layer. Hence, the transmission is negligible, and the absorption coefficient comes out to be $A(\omega) = 1 - R(\omega)$.

The comparison between the absorption performance of the inner graphene resonator (IG), outer graphene resonator (OG), and their combination (IG + OG) is shown in figure 2. As seen, the IG resonator only provides poor performance in terms of absorption, with a maximum absorption value equal to approximately 43% at 2.2 THz. On the other hand, the absorption of the OG resonator reaches values nearly equal to 99% in the frequency region of 2.25–2.6 THz. By combining the two resonators, the absorption performance is improved especially on the low-frequency side of the operation frequency band. Thus, at 2 THz, absorption changes from about 0.8 (OG) to 0.9 (IG + OG).

Also, the overall design helps maintain a higher level of absorption around 90% within the 2–2.93 THz range, leading to an enhanced and stable absorption characteristic. Likewise, the absorption at 2.93 THz has been increased from 83% with the OG structure to over 90% with the IG + OG combination design. Such findings show that electromagnetic coupling between the inner and OG resonators produces extra resonances that combine with one another and lead to the broadband absorption feature of the designed absorber. Hence, the effect of the inner resonator on the absorption characteristic can be insignificant as far as the peak absorption value is concerned; however, it plays a key role in achieving broadband absorption.



(a) TE spectral plot

(b) TM spectral plot

Figure 3. Effect of azimuth angle on absorptivity.

2.2. Polarization insensitivity and angular stability

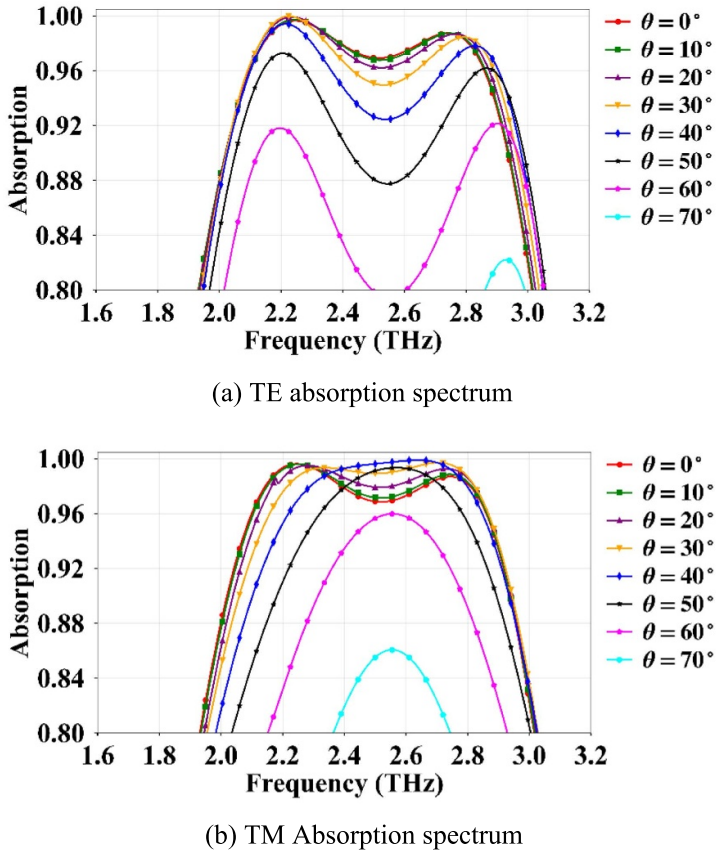
As shown in figure 3, the absorption characteristics of the proposed absorber are evaluated for different azimuth angles (φ) under both TE and TM polarizations. The absorption spectra are observed to almost completely overlap over the entire azimuth range from 0° to 90°, indicating that the absorber is insensitive to azimuthal angle variations. In addition, the nearly identical responses for TE and TM polarizations confirm the polarization-insensitive behavior of the proposed design.

The variation of absorptivity with respect to different incident angles for both TE and TM modes is shown in figure 4. As can be seen in figure 4(a), the effective absorption bandwidth for small incident angles ($\theta \leqslant 50°$) according to the criterion of 90% absorption rate does not change much, suggesting consistent broadband performance. But when the incident angle becomes higher, the bandwidth gradually becomes smaller, mostly attributed to the decrease of the upper cutoff frequency. When the incident angle exceeds 50°, a great bandwidth drop can be observed, making the absorber exhibit narrowband performance. In high angles ($\theta \geqslant 70°$), the absorber seldom reaches a 90% absorption rate, implying the lack of broadband absorption.

As can be seen from figure 4(b), the absorber demonstrates a broad absorption bandwidth ($A \geqslant 90\%$) over incident angles below 30°, which clearly shows its robustness against angular variation in TM polarization. As the incident angle increases, there is an obvious decrease in the bandwidth because of the lower cut-off frequency. For large incident angles ($\theta \geqslant 60°$), the effective bandwidth reduces greatly since the absorption does not exceed 90%. However, in comparison with the TE polarization, the TE polarization performs better in terms of bandwidth conservation under moderate incident angles.

2.3. E-field analyses of the proposed absorber

The electric field distributions of the designed absorber at different frequencies have been shown in figure 5. It can be seen that at the frequencies in the operating range (2–2.93 THz), the presence of electric field concentration mainly takes place in the vicinity of the edge and gap portions of the resonators, signifying the existence of the electric dipole and LC resonances. This results in high energy confinement along with effective impedance matching to free space for achieving near unit absorptivity. Conversely,



(a) TE absorption spectrum

(b) TM Absorption spectrum

Figure 4. Effect of the incident angle on the absorptivity.

outside the operational frequency band, the field distribution is not so strong and localized, thus no significant resonance, implying low absorptivity.

2.4. Analysis of surface current distribution

Figure 6 presents the surface current distributions of the proposed absorber at different frequencies. Strong current concentrations are observed along the edges of both graphene resonators within the operating band (2–2.93 THz), indicating the excitation of resonant modes and effective confinement of electromagnetic energy. For low frequencies, the outer resonator plays the major role in defining the resonating behavior, while the inner resonator plays the dominant role for high frequencies. For the medium frequency values, both resonators are involved in the flow of currents, thereby generating various resonant modes. This interaction between resonances increases the absorption bandwidth, leading to absorptions higher than 90% within the complete operation frequency band. At regions outside the operational frequency band, there is a significant reduction in the current magnitude.

2.5. Impedance matching characteristics of the proposed absorber

To elucidate the operating mechanism of the proposed metamaterial absorber, the normalized input impedance was calculated from the simulated reflection coefficient using the following equation [9, 24]:

$$Z_r(\omega) = \sqrt{\frac{(1+S_{11})^2 - S_{21}^2}{(1-S_{11})^2 - S_{21}^2}} \tag{2}$$

where S_{11} and S_{21} represent reflection and transmission coefficients, respectively. The impedance matching characteristics were subsequently analyzed to explain the near-perfect absorption behavior. For efficient absorption, the normalized impedance should approach that of free space, corresponding to $\mathrm{Re}(Z_r) \approx 1$ and $\mathrm{Im}(Z_r) \approx 0$. The normalized impedance of the designed absorber is shown in figure 7. It can be seen from the selected frequency range (2–2.93 THz) that the real value of the normalized impedance is nearly equal to unity, and the imaginary value of the same tends towards zero for certain frequencies, while staying relatively low in the rest of the band. This implies that there is excellent impedance matching of the absorber with free space, resulting in absorption rather than reflections.

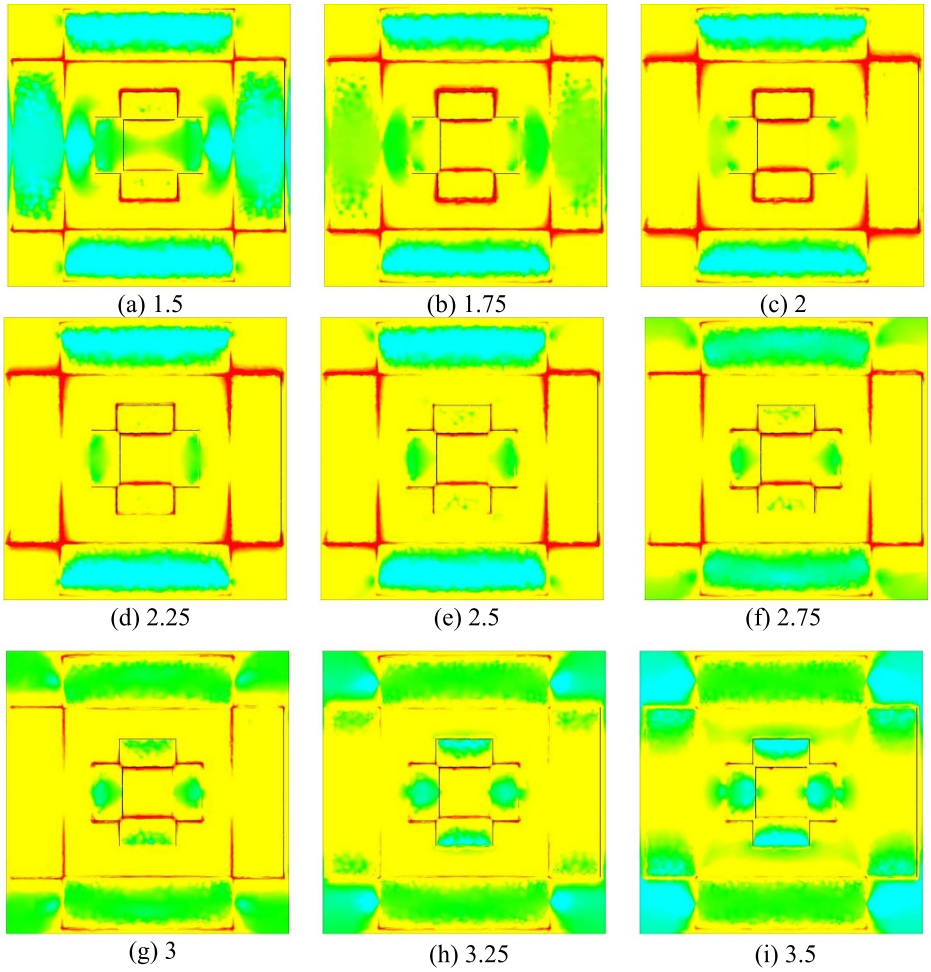


Figure 5. Frequency-dependent electric field distribution of the proposed absorber.

Thus, high broadband absorption of more than 90% is due to both impedance matching and resonant losses.

2.6. Tolerance analysis

In order to verify the performance stability of the proposed absorber against fabrication uncertainties, a tolerance analysis was carried out. The chemical potential of the graphene layer (μ_c), together with the geometrical parameters *a, b, c,* and *d,* were individually varied by ±10% around their optimized values, whereas the periodicity *p* was varied by ±5%. During each analysis, all remaining parameters were kept fixed. The results indicate that the proposed absorber is generally robust against fabrication-induced variations. While the absorption response shows some sensitivity to variations in μ_c and *d*, only minor changes are observed for *a, b, c,* and *p*, confirming the good tolerance characteristics of the proposed design.

The absorption characteristics of the suggested absorber based on varying graphene chemical potential levels are presented in figure 8. It can be seen that the absorption characteristics are highly sensitive to the level of graphene chemical potential. In the case of $\mu_c = 0.70$ eV, the absorber presents the narrowest absorption range, where the value of absorption is lower than 90%. This suggests that with a lower level of chemical potential, the conductivity of graphene becomes smaller, which in turn makes its resonance weaker. With increasing values of chemical potential, the absorption band shifts to higher frequencies, demonstrating the tunable nature of the graphene resonators. Of all investigated values, $\mu_c = 0.90$ eV presents optimal absorption performance in the working band. At this value of chemical potential, the absorber operates at almost 99% absorption rate across a broad spectrum of frequencies, and at the same time, retains its broadband operation. As mentioned above, $\mu_c = 0.80$ eV also gives the same absorption values, but $\mu_c = 0.90$ eV produces more favorable absorption performance in the working band and shifts the region of high absorption rates to higher frequencies. If one increases the value of chemical potential to 1.00 eV, then absorption in mid-bands decreases. Thus, it is confirmed

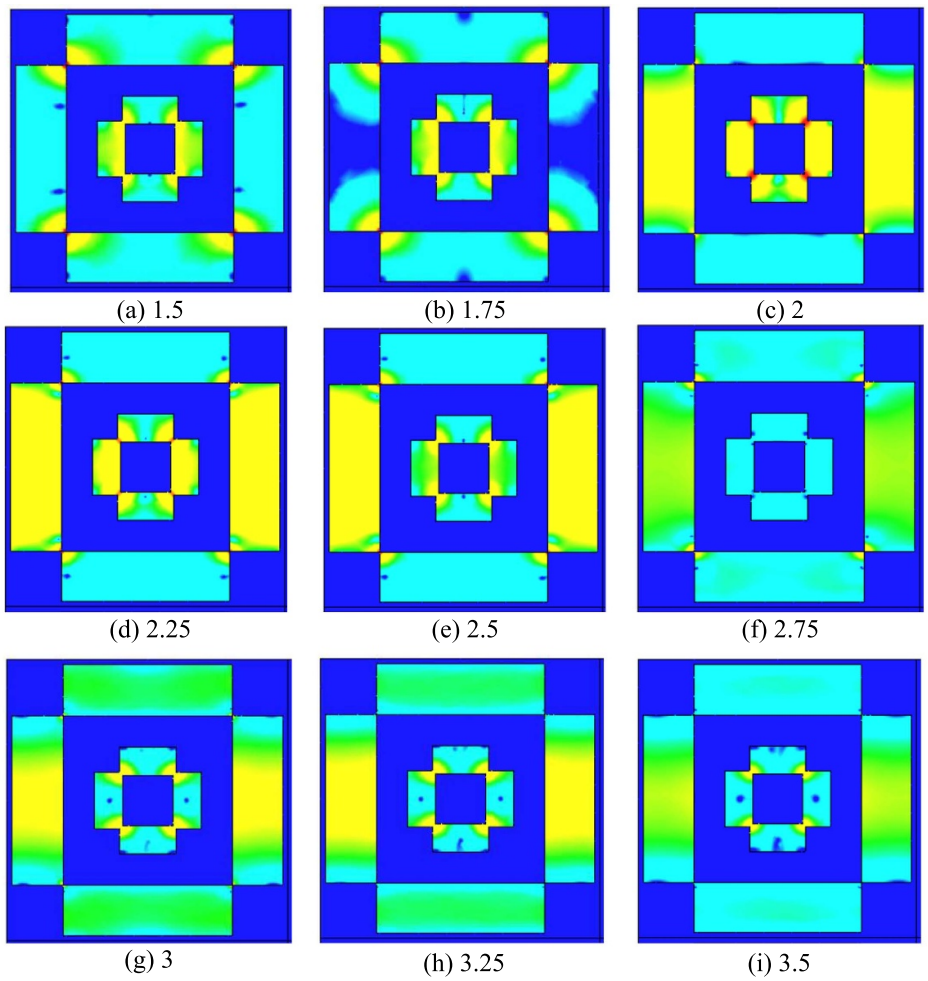


Figure 6. Surface current distribution at different frequencies.

that absorption properties of the proposed absorber can be efficiently controlled by varying its chemical potential.

Figure 9 illustrates the influence of the a parameter on the absorption efficiency of the absorber. A fabrication tolerance analysis was carried out using variations in the value of a between 0.9 μm and 1.1 μm with respect to the baseline of 1 μm, representing $\pm$10%. It can be noticed that all considered structures exhibit a very high level of absorption efficiency regardless of the value of a. Despite some deviation from the baseline in the absorption response curves for different values of a, no major changes have been detected regarding the absorption properties. In particular, $a = 1\,\mu$m shows the most uniform absorption behavior and gives the highest value of average absorption among the considered parameters. This suggests that $a = 1\,\mu$m can be considered the optimal value for the considered parameter. These findings confirm that the proposed absorber is robust against reasonable fabrication-induced deviations in parameter a.

The impact of parameter b on the absorption behavior of the designed absorber is depicted in figure 10. The tolerance analysis was performed by changing b from 1.8 μm to 2.2 μm, which corresponds to $\pm$10% variation from its optimal value of 2 μm. It is seen from the figure that all tested designs have a highly absorptive behavior in the frequency band. This proves that the design is tolerant of $\pm$10% dimensional variations of the parameter. However, some significant differences were found in the middle-band range between 2.4 and 2.6 THz. Namely, the absorptive properties degrade in the case of $b = 1.8\,\mu$m, but the absorber with $b = 2\,\mu$m shows more uniform behavior along the entire frequency band. In addition, although $b = 2.2\,\mu$m increases the absorption level in low-frequency ranges, a decrease can be observed in mid-frequency ranges. The best tradeoff is obtained for the optimal value $b = 2\,\mu$m; thus, it will be considered in further investigations. These results confirm that the proposed absorber maintains stable performance under $\pm$10% dimensional variations of parameter b.

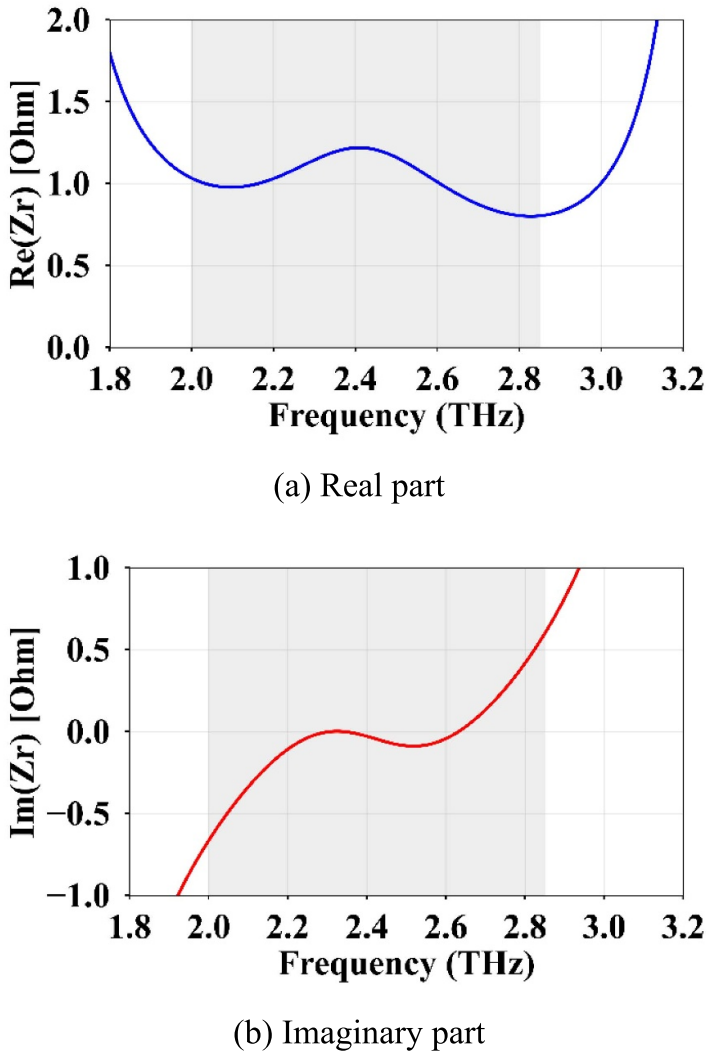


Figure 7. Frequency-dependent normalized impedance of the proposed absorber.

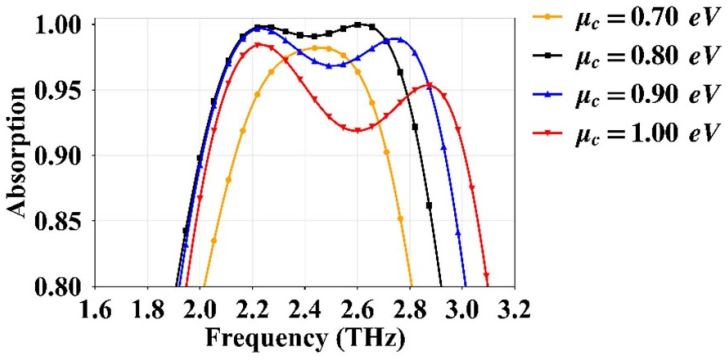


Figure 8. Absorption characteristics of the proposed absorber for different graphene chemical potential values.

The influence of the c parameter on the absorption properties of the proposed absorber is shown in figure 11. To conduct a sensitivity analysis, changes in c in the range from 1.62 μm to 1.98 μm were considered, where $\pm$10% variation in the parameter relative to the nominal value of 1.8 μm is involved. From the analysis of the results, it can be seen that there is moderate sensitivity of the absorption properties of the proposed absorber to changes in the c parameter in the middle frequency range of 2.4–2.7 THz. In particular, for lower values of this parameter, namely 1.62 μm and 1.71 μm, the absorption spectrum is rather flat and the level of absorption almost reaches 100% in most of the operating

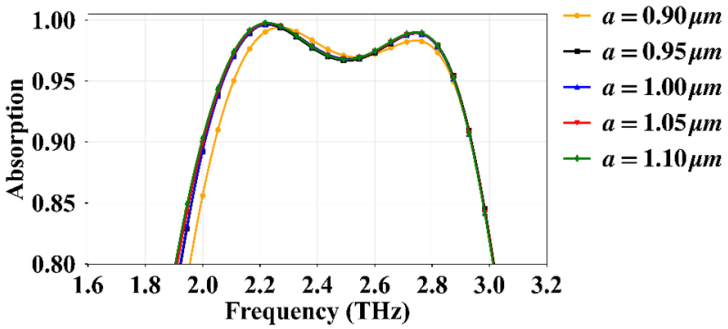


Figure 9. Absorption characteristics of the proposed absorber for different *a* values.

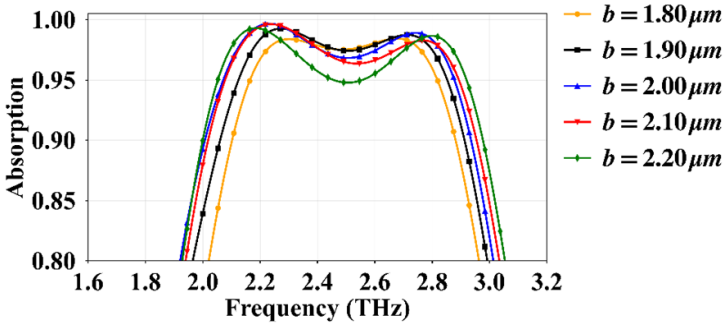


Figure 10. Absorption characteristics of the proposed absorber for different *b* values.

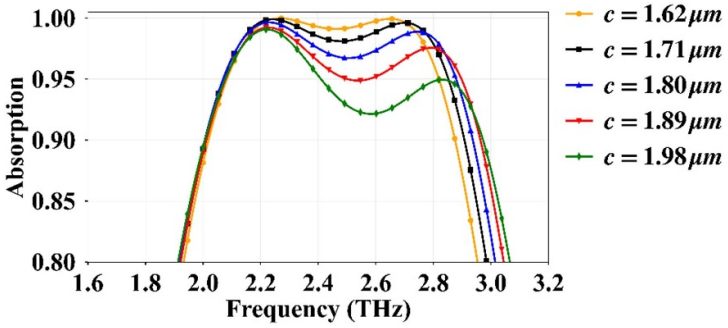


Figure 11. Absorption characteristics of the proposed absorber for different *c* values.

frequency band. For larger c values than nominal ones, absorption drops off significantly in the middle of the working band. However, despite this, the absorption level in all cases remains high enough to demonstrate high robustness against possible fabrication errors. These results confirm that the proposed design can tolerate $\pm$10% deviations in parameter c without significant degradation of its overall absorption performance.

The effect of parameter d on the absorption characteristics of the presented absorber structure is shown in figure 12. The sensitivity study for the tolerance analysis is done for variations of d between 5.4 μm and 6.6 μm, which are $\pm$10% variations relative to its nominal value 6 μm. As seen from the simulation outcomes, parameter d plays an important role in affecting the absorption performance and resonance mode interactions. It has been found that low values of d (5.4 μm and 5.7 μm) lead to a split of absorption peaks, causing a considerable decline in the absorption rate in the mid-frequency range. An increase of d toward its nominal value, 6 μm, enhances resonance interactions, which in turn leads to wider and more uniform absorption bandwidth with high absorption rates higher than 96%. However, as soon as d further increases (6.3 μm and 6.6 μm), a poor absorption response can be seen in the mid-frequency range because of changes in resonance interactions. In summary, $d = 6\,\mu$m is the

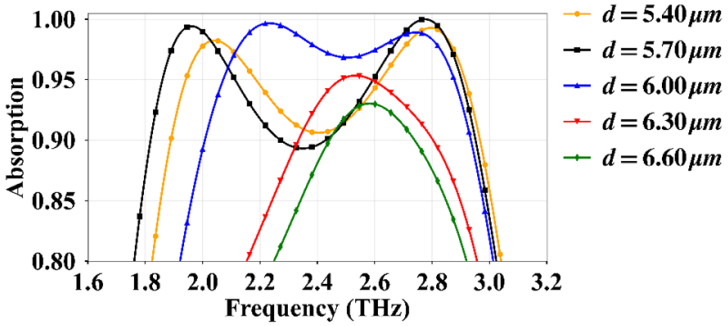


Figure 12. Absorption characteristics of the proposed absorber for different d values.

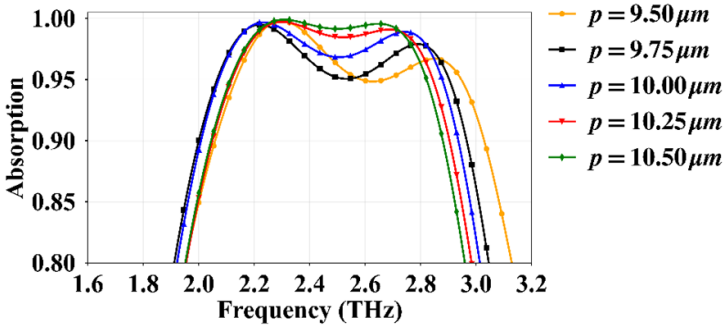


Figure 13. Effect of unit-cell periodicity variation on the absorption performance of the proposed absorber.

optimal parameter value providing good performance of the absorber, and the absorber exhibits higher sensitivity to variations in parameter d compared to the other geometrical parameters.

The fabrication tolerance analysis of the unit-cell periodicity p is illustrated in figure 13. The periodicity was varied between 9.5 μm and 10.5 μm, or equivalently $\pm$5% around the nominal period of 10 μm. As can be seen, all studied cases show excellent performance with regard to the achieved broadband absorption. Although the reduction of periodicity to 9.5 μm leads to a slight decrease in absorption at the mid-frequencies, the broadband absorption is still greater than 95%. With the increase in periodicity up to 10.25 μm and 10.5 μm, the achieved broadband absorption becomes more flat and the percentage of absorption exceeds 98%. On the other hand, one should note that even for the nominal case of $p = 10\,\mu$m, excellent broadband absorption is achieved. The results illustrate the ability of the designed absorber to sustain dimensional tolerance of $\pm$5% for the unit-cell periodicity.

In general, the tolerancing analysis proves the reliability of the designed absorber under fabrication uncertainties. The analysis demonstrates that variation in the values of geometrical parameters a, b, and c up to $\pm$10%, and periodicity p up to $\pm$5% does not significantly affect the absorber's behavior. In this way, the manufacturing of this device can be performed without much problem in terms of tolerances of these parameters. However, the chemical potential of graphene (μ_c) and parameter d play an important role in the absorber's absorption behavior. This is due to the fact that parameter d plays an important role in the coupling between the two resonators, whereas μ_c impacts the conductivity of graphene directly.

2.7. Refractive index sensing analysis

To evaluate the refractive index sensing capability of the proposed terahertz absorber, an analyte layer was introduced on the top surface of the structure. Variations in the refractive index modify the effective dielectric environment surrounding the resonator, resulting in resonance frequency shifts. Owing to the strong confinement of the electromagnetic field within the analyte region, even small refractive index variations produce measurable changes in the resonance characteristics. The refractive index was varied from 1.0 to 2.0, while the analyte thickness was investigated from 0.2 μm to 1.0 μm in increments of 0.2 μm.

Figure 14 presents the absorption spectra for different refractive indices at an analyte thickness of 1 μm. Two resonance modes are observed at approximately 2.1 THz and 2.7 THz. The lower-frequency

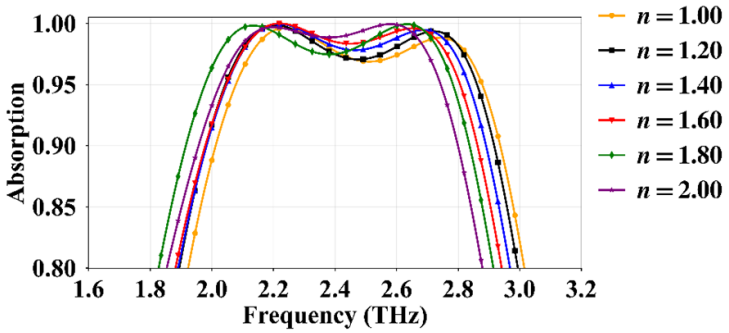


Figure 14. Absorption spectra of the proposed sensor at an analyte thickness of 1 μm for different refractive indices.

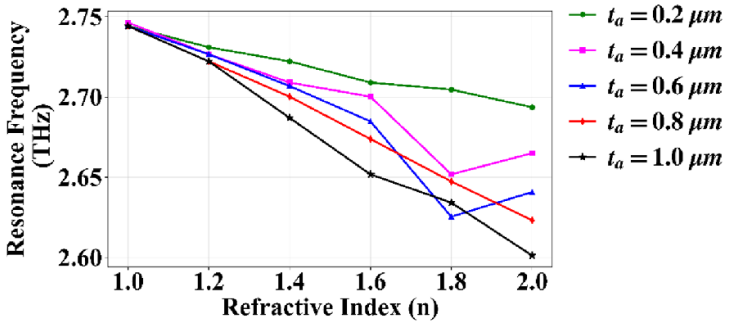


Figure 15. Resonance frequency shift as a function of refractive index for different analyte thicknesses.

resonance does not exhibit a consistent frequency shift with increasing refractive index. However, the higher-frequency resonance undergoes a clear and continuous shift. Hence, the second resonance is chosen to assess the sensing capability of the designed structure. This shift is due to the increment in the effective dielectric constant of the analyte.

Resonance frequency behavior of the second resonance mode as a function of analyte thickness is illustrated in figure 15. An increase in the refractive index results in the lowering of the resonance frequency for any given thickness of the analyte. Moreover, the magnitude of the frequency shift becomes more pronounced as the analyte thickness increases which indicates stronger interaction between the localized electromagnetic field and the analyte layer. For example, when the analyte thickness is increased to 1.0 μm, the resonance frequency shifts from 2.744 THz to 2.601 THz which one corresponding to the maximum frequency shift of 0.143 THz. An analyte thickness of 0.2 μm leads to the minimum frequency shift of around 0.051 THz. Moreover, responses for 0.8 μm and 1.0 μm analyte thicknesses show better linearity with respect to refractive index. Taking into account the frequency shift, sensitivity, FOM, and Q factor, the 1.0 μm analyte thickness was considered as the optimum sensing configuration for subsequent analyses.

The sensing performance was evaluated using sensitivity (S), full width at half maximum (FWHM), figure of merit (FOM), and quality factor (Q). The sensitivity is defined as the resonance frequency shift per unit change in refractive index and is calculated using equation (3) [25–27].

$$S = \frac{\Delta f}{\Delta n} \tag{3}$$

where Δf is the resonance frequency shift and Δn is the refractive index variation. Higher sensitivity indicates a stronger response to small refractive index changes. FWHM represents the bandwidth of the resonance peak measured at half of its maximum amplitude. A smaller FWHM corresponds to a sharper resonance peak, enabling more accurate determination of resonance frequency shifts and consequently improving sensing resolution. The FOM, calculated using equation (4), combines the effects of sensitivity and resonance linewidth [25–27].

$$\mathrm{FOM} = \frac{S}{\mathrm{FWHM}}. \tag{4}$$

Table 2. Refractive index detection performance of the proposed terahertz graphene absorber.

$n1$	$n2$	Δf (THz)	Δn	S (GHz/RIU)	FWHM (THz)	FOM (RIU^{-1})	Q
1.0	1.2	0.022	0.2	110	0.257	0.427	10.661
1.2	1.4	0.0352	0.2	176	0.251	0.702	10.854
1.4	1.6	0.0352	0.2	176	0.244	0.721	11.003
1.6	1.8	0.0176	0.2	88	0.235	0.374	11.265
1.8	2.0	0.033	0.2	165	0.227	0.728	11.625
Average				143	0.243	0.590	11.082

Table 3. Effect of analyte thickness on the sensing performance of the proposed sensor.

t_a (μm)	f (THz)	S (THz/RIU)	FWHM (THz)	FOM (RIU^{-1})	Q
0.2	2.717	0.051	0.251	0.202	10.838
0.4	2.700	0.081	0.246	0.330	10.964
0.6	2.688	0.103	0.243	0.425	11.055
0.8	2.685	0.121	0.241	0.502	11.150
1	2.673	0.143	0.238	0.601	11.266

A higher FOM indicates that the sensor simultaneously possesses high sensitivity and narrow resonance characteristics, resulting in superior sensing performance. The quality factor (Q) is another important parameter describing the sharpness of the resonance peak and is determined using equation (5) [25–27].

$$Q = \frac{f_r}{\text{FWHM}}. \tag{5}$$

Higher Q values indicate narrower resonance peaks and greater frequency selectivity, which improve the accuracy of resonance shift detection. Table 2 summarizes the sensing performance of the proposed sensor for an analyte thickness of 1 μm. The sensitivity varies from 88 to 176 GHz RIU^{-1}, with an average value of 143 GHz RIU^{-1}. As the refractive index increases, the FWHM decreases from 0.257 THz to 0.227 THz, indicating progressively sharper resonance peaks. Consequently, the Q factor increases from 10.661 to 11.625, while the highest FOM of 0.728 RIU^{-1} is achieved for the refractive index interval of 1.8–2.0. These results demonstrate that the proposed sensor combines high sensitivity with excellent resonance selectivity.

The influence of analyte thickness on sensing performance is summarized in table 3. Increasing the analyte thickness enhances the interaction between the electromagnetic field and the analyte, resulting in larger resonance frequency shifts. Accordingly, the sensitivity increases from 0.051 THz RIU^{-1}–0.143 THz RIU^{-1}, while the FWHM decreases from 0.251 THz to 0.238 THz. This improvement is accompanied by corresponding increases in both the Q factor (10.838–11.266) and the FOM (0.202–0.601 RIU^{-1}). Among all investigated thicknesses, the 1.0 μm analyte layer provides the highest sensitivity, FOM, and Q factor, demonstrating that it is the optimum sensing configuration for the proposed terahertz graphene absorber.

Overall, the proposed sensor exhibits excellent refractive index sensing performance, achieving an average sensitivity of 143 GHz RIU^{-1} together with high FOM and Q values. These characteristics demonstrate that the proposed graphene absorber is a promising candidate for high-performance terahertz refractive index sensing applications.

2.8. Fabrication considerations and practical realization

Although the performance of the designed absorber has been verified through numerical simulations, its practical realization can be readily achieved using state-of-the-art microfabrication technologies. The structure features a straightforward three-layer configuration: a continuous copper ground plane, an Arlon 1000D dielectric spacer, and patterned graphene resonators. Since the proposed structure does not require complex multilayer designs or complicated three-dimensional shapes, it can be fabricated using standard batch-fabrication techniques commonly used for terahertz devices. The fabrication process starts with the preparation of the Arlon 1000D dielectric substrate. The substrate is selected or polished to the required thickness to provide the desired spacing between the ground plane and the top resonator layer. A continuous copper layer can be deposited on the back side of the substrate using common deposition methods such as magnetron sputtering or electron-beam evaporation. This layer acts as

Table 4. Comparative evaluation of the proposed THz absorber.

References	Year	Size (um^3)	Size ($\lambda^3{}_0$)	Layers	Absorption > 90% bandwidth (THz)	Bandwidth (THz)	Relative bandwidth (%)
This work	2026	10 × 10 ×9.915	0.067 × 0.067 × 0.066	3	2–2.93	0.93	37.72
[9]	2025	32 × 32 × 12.5	0.739 × 0.739 × 0.289	5	6.93–10.16	3.23	37.8
[28]	2025	10.1 ×10.1 × 8.91	0.140 × 0.140 × 0.120	5	4.08–35.25	31.17	158.5
[10]	2025	58 × 58 × 15.3	0.340 × 0.340 × 0.090	3	1.75–4.85	3.1	93.9
[11]	2025	27 × 27 × 10.6	0.310 × 0.310 × 0.120	3	3.44–8.37	4.93	83.4
[12]	2025	100 × 100 × 14	0.32 × 0.320 × 0.045	3	0.97–2.19	1.22	77.2
[13]	2025	18 × 18 × 8.38	0.170 × 0.170 × 0.080	3	2.82–9.17	6.35	105.9
[17]	2024	30 × 30 × 12.36	0.290 × 0.290 × 0.120	5	2.9–12.44	9.54	124.4
[18]	2024	12 × 12 × 5.201	0.130 × 0.130 × 0.058	3	3.34–3.98	0.64	17.5
					4.60–5.30	0.7	14.1
[29]	2024	6.5 × 6.5 × 40.5	0.100 × 0.100 × 0.640	3	4.70–6.70	2	35.1
[30]	2024	30 × 30 × 8.80	0.420 × 0.420 × 0.120	3	4.20–5.80	3.3	32
[19]	2023	10 × 10 × 9.915	0.107 × 0.107 × 0.106	3	3.20–5.32	2.12	50
[31]	2025	23 × 23 × 11	0.038 × 0.038 × 0.018	5	0.50–3.50	3	150
					4.00–5.00	1	22.2

the ground plane. Next, a high-quality single-layer graphene sheet grown by chemical vapor deposition can be transferred onto the top surface of the substrate using standard transfer techniques. Since the unit cell has micro-scale dimensions, a smooth and flat surface is important for accurate patterning. After the graphene transfer, photolithography or electron-beam lithography can be used to create the desired resonator patterns. Finally, oxygen plasma reactive-ion etching is applied to remove unwanted graphene and form the inner and OG resonators accurately. The proposed absorber has a simple geometry that mainly consists of rectangular graphene structures. Therefore, it is less sensitive to fabrication errors than designs with complex fractal shapes or multilayer structures. The compact unit-cell size and fully planar design make it easy to integrate with existing terahertz devices, waveguides, and sensing systems. In addition, graphene provides the benefit of tunability after fabrication. By applying an external bias voltage, the Fermi energy (chemical potential) of graphene can be adjusted. As a result, the absorption properties of the device, such as the resonance frequency and absorption strength, can be controlled in real time without changing the physical structure. This feature makes the absorber suitable for reconfigurable terahertz devices and smart sensing applications. Because of its simple geometry, small number of layers, and well-established graphene fabrication methods, the proposed absorber is highly suitable for experimental realization and practical terahertz applications.

2.9. Comparison of the proposed absorber with similar absorbers

Table 4 presents a comparison of the proposed terahertz metamaterial absorber structure with current studies in the literature. Examination of the comparison results shows that some studies provide wider absolute bandwidth and higher relative bandwidth. However, it should be noted that many of these structures have multilayered configurations, hybrid materials like VO_2-graphene, or larger cell sizes. The suggested structure has normalized parameters $0.067\lambda_0 \times 0.067\lambda_0 \times 0.066\lambda_0$. The proposed structure exhibits one of the smallest normalized volumes among the compared THz absorbers, making it highly attractive for compact and integrated terahertz applications. Besides, the considered structure has three layers and does not involve complicated multilayer or fractal geometries.

It also enables the design to be fabricated and implemented for practical uses. Nonetheless, the suggested absorber has shown to absorb over 90% energy in the 2–2.93 THz frequency range by giving a bandwidth of 0.93 THz and a relative bandwidth of 37.72%. While there have been other reports where higher bandwidths were obtained, the most prominent feature of the suggested design lies in achieving wide bandwidth absorption despite having very small size dimensions. Consequently, rather than aiming for the highest bandwidth, the proposed study offers a balanced design approach between compactness, structural simplicity, and wideband absorption performance. Thanks to these features, the proposed absorber constitutes a significant alternative for integrated THz systems, sensing applications, and miniaturized electromagnetic components where size constraints are critical.

3. Conclusions

This study presents the design and numerical investigation of a compact broadband graphene-based terahertz metamaterial absorber. It possesses a very small volume of around $0.067\lambda_0 \times 0.067\lambda_0 \times 0.066\lambda_0$, and, thus, making it one of the most compact graphene-based THz absorbers reported in the literature. It achieves an absorption level higher than 90% over the frequency range of 2–2.93 THz corresponding to an absolute bandwidth of 0.93 THz and a relative bandwidth of 37.72%. Absorption properties were examined through studies based on electric field distributions, surface current distributions, and impedance-matching properties. The findings clearly indicated that broad absorption is realized due to the combination of several resonant states along with the efficient impedance-matching process between the absorber and the free space. Moreover, the absorber is polarization-independent, and maintains broadband absorption for incident angles up to 50° in TE polarization and up to 30° in TM polarization. A thorough tolerance analysis was carried out by considering ±10% variations in μ_c and the geometrical parameters *a, b, c*, and *d*, while the periodicity *p* was varied by ±5%. It is found that the absorber shows high tolerance to any parameter variation in terms of *a, b, c*, and *p*, while the absorptivity shows a greater sensitivity to μ_c and *d*. Nevertheless, the absorber preserves its broadband absorption performance under reasonable fabrication-induced deviations. Moreover, for an analyte thickness of 1 μm, the proposed absorber also demonstrated multifunctional capability by operating as a refractive-index sensor with an average sensitivity of 143 GHz RIU^{-1}, an average FOM of 0.590 RIU^{-1}, and an average *Q*-factor of 11.082. It proves that the suggested device can be used for various applications including absorption and sensing applications within the THz band range. Therefore, the proposed design offers an effective balance between compactness, structural simplicity, broadband absorption, fabrication feasibility, and sensing capability, making it a promising candidate for next-generation integrated THz systems.

Data availability statement

The data that support the findings of this study are available from the corresponding author upon reasonable request. Due to the nature of this research, some data (including simulation files and experimental setup details) are not publicly available but can be shared for academic purposes.

The data cannot be made publicly available upon publication because no suitable repository exists for hosting data in this field of study.

Funding statement

This research did not receive any specific grant from funding agencies in the public, commercial, or not-for-profit sectors.

Conflict of interest

On behalf of all authors, the corresponding author states that there is no conflict of interest.

Ethics statement

This study does not involve human participants or animals. Therefore, ethical approval and informed consent were not required.

Author contribution

Kayhan Çelik 0000-0003-0371-0473
Conceptualization (equal), Methodology (equal), Supervision (equal), Validation (equal), Visualization (equal), Writing – original draft (equal)

References

[1] Punia T and Malik H K 2023 Multifocal THz emission with multiple resonances *Trans. Electromagn. Spectr.* **2** 25–32
[2] Çelik K, Kurt E and Korkmaz O 2025 A novel multiple-slot pixel patch antenna for wideband terahertz applications *JOM* **77** 2967–75
[3] Teksar A Y 2022 Crescent-shaped monopole antenna for WLAN band *Trans. Electromagn. Spectr.* **1** 1–4
[4] Fuscaldo W, Negri E, Maita F, Maiolo L, Beccherelli R and Zografopoulos D C 2025 Modal and reflective properties of capacitive and inductive terahertz metasurfaces *Adv. Opt. Mater.* **13** e01605
[5] Pan H and Zhang H-F 2021 Broadband polarization-insensitive coherent rasorber in terahertz metamaterial with enhanced anapole response and coupled toroidal dipole modes *Adv. Opt. Mater.* **10** 2101688
[6] Omole O V, Gbenro S O, Oludare E O and Agbele A T 2024 Analysis and characterization of inter-events of Ku-band satellite signals over a mountainous region in Ikere-Ekiti, Nigeria *Trans. Electromagn. Spectr.* **3** 59–66
[7] Shui W, Li J, Wang H, Xing Y, Li Y, Yang Q, Xiao X, Wen Q and Zhang H 2020 Ti3C2Tx MXene sponge composite as broadband terahertz absorber *Adv. Opt. Mater.* **8** 2001120
[8] Oladiran S O and Adedeji K B 2026 Analysis of a compact UWB antenna with integrated band-notched feature for wireless body area network applications *Trans. Electromagn. Spectr.* **5** 1–11
[9] Xianhua Y, Wang Y, Tang L, Zhang H and Wang Y 2025 Dynamically tunable terahertz metamaterial absorber with triple narrowband and broadband absorption *Physica B* 417737
[10] Wei Z, Yi Y, Yang H, Yi Z and Yi Y 2025 Adjustable broadband terahertz metamaterial absorber with a single layer graphene structure made base on the principle of strong electric field coupling *Micro Nano Struct.* **207** 208297
[11] Kumar S and Rao V S 2025 Design and simulation investigations of ultrawideband metamaterial-based terahertz absorber *IEEE Trans. Plasma Sci.* **53** 3205–11
[12] Mohammed M M, Awl H N, Rashid Z M, Mahmud R H and Abdulkarim Y I 2025 Simulated study of a broadband terahertz metamaterial absorber based on vanadium dioxide resonator for cancer detection applications *Plasmonics* 1–12
[13] Wang Y, Chen Y, Liu F, Chen L, Ji K, Wang X and Ji X 2025 Vanadium dioxide enabled polarization insensitive tunable broadband terahertz metamaterial absorber *Sci. Rep.* **15** 10140
[14] Bhatt P, Jain P and Joshi A 2026 Deep learning-assisted ultrathin broadband vanadium dioxide-based polarization-insensitive terahertz metamaterial absorber *Sci. Rep.* **16**
[15] Vasu Babu K, Sree G N J, Das S, Islam T, Algarni A D and Ghzaoui M E L 2026 Theoretical investigation and ML-based optimization of a thermally tunable metamaterial absorber using vanadium dioxide (VO_2) for terahertz biomedical sensing and cancer cell detection *Int. J. Therm. Sci.* **227** 110917
[16] Mishra A, Vishwakarma R, Srivastava K V, Chauhan Y S and Verma A 2026 Frequency reconfigurable absorber using a uniform vanadium dioxide film-based substrate thickness modulator *J. Appl. Phys.* **59** 115302
[17] Zhang Y, Sun X, Li Z, Liu L and Qin G 2024 Ultra-wideband terahertz metamaterial absorber with polarization insensitivity and broad incidence angle absorption *Phys. Scr.* **100** 015531
[18] Rekha V S D, Prasad N, Madhav B and Alathbah M 2024 Design and analysis of Minkowski fractal shaped metasurface absorber with broadband and polarization-insensitive characteristics using a tunable graphene layer for terahertz applications *Phys. Scr.* **99** 085934
[19] Chao X, Xu Y, Huang F and Chen Z 2023 A high-quality broadband tunable terahertz metamaterial absorber based on graphene *J. Appl. Phys.* **57** 075106
[20] Jornet J M and Akyildiz I F 2014 Graphene-based plasmonic nano-antenna for terahertz band communication in nanonetworks *IEEE J. Sel. Areas Commun.* **31** 685–94
[21] Asgari S and Fabritius T 2024 Multi-band terahertz metamaterial absorber composed of concentric square patch and ring resonator array *Opt. Contin.* **3** 148–63
[22] Asgari S and Fabritius T 2023 Numerical simulation and equivalent circuit model of multi-band terahertz absorber composed of double-sided graphene comb resonator array *IEEE Access* **11** 36052–63
[23] Çelik K 2026 Polarization-insensitive, ultrathin, miniaturized, broadband graphene-based terahertz metamaterial absorber *Opt. Quantum Electron.* **58**
[24] Wu G, Li C, Wang D, Chen W, Gao S, Guo H, Zhang C and Guo S 2023 Terahertz absorber with switchable functionality from ultra-broadband to broadband *Diam. Relat. Mater.* **139** 110306
[25] Shangguan Q, Chen Z, Yang H, Cheng S, Yang W, Yi Z, Wu X, Wang S, Yi Y and Wu P 2022 Design of ultra-narrow band graphene refractive index sensor *Sensors* **22** 6483
[26] Nejat M and Nozhat N 2019 Ultrasensitive THz refractive index sensor based on a controllable perfect MTM absorber *IEEE Sens. J.* **19** 10490–7
[27] Nickpay M-R, Danaie M and Shahzadi A 2021 Highly sensitive THz refractive index sensor based on folded split-ring metamaterial graphene resonators *Plasmonics* **17** 237–48
[28] Cui M, Zhang G, Bi K, Xing B, Diao G, Du Y, Ge Z and Zhang Y 2025 Polarization-insensitive ultra-broadband terahertz metamaterial absorber using vanadium dioxide and graphene *Phys. Lett. A* **552** 130632
[29] Mazaheri M H, Maab H and Rahim A A 2024 Graphene-based metamaterial absorber for energy harvesting in the terahertz range *J. Opt.* **53** 4751–61
[30] Asrafali B, Khan F, Pavithra M, Rani R, Zheng Y and Yogesh N 2024 Sierpinski metamaterial for near-perfect terahertz tunable broadband absorber using vanadium dioxide *2024 Prog. Electromagn. Res. Symp. (PIERS)* (IEEE) (https://doi.org/10.1109/piers62282.2024.10618731)
[31] Javadifar N, Ghoreishi Amiri S S, Yousefi R, Adarang H and Dehbovid H 2025 Bi-functional THz wave absorber based on periodic arrays of graphene pattern *Indian J. Phys.* 1–8